Memoirs of the Faculty of Science, Kyoto University, Series of Physics, Astrophysics, Geophysics and Chemistry, Vol. XXXVI, No. 1, Article 2, 1981

NEUTRAL PION PHOTOPRODUCTION FROM HYDROGEN AT FORWARD ANGLES IN THE ENERGY REGION BETWEEN 450 MEV AND 975 MEV

By

Akira NODA*

Department of Physics, Kyoto University Kyoto, Japan

(Received February 6, 1979)

ABSTRACT

The differential cross sections of the reaction $\gamma+p\rightarrow\pi^{\circ}+p$ in the energy region between 450 MeV and 975 MeV in the angular range of the pion emission angle from 15° to 130° in the CM system have been measured by two different detection systems. The detection system for the measurement at forward angles from 15° to 50° was a π°-counter, which detected two decayed photons from a π° meson. For the measurement at backward angles from 50° to 130°, a magnetic spectrometer was used in coincidence with a photon detector. This paper describes details of the measurement with the π°-counter. The results are compared with the phenomenological analyses by Metcalf and Walker (MW) and Moorhouse, Oberlack and Rosenfeld (MOR). At the forward angles (15° and 35°), the present results are higher than these analyses in the energy region below 600 MeV. A calculation based on fixed-t dispersion relation and with the resonance saturation of imaginary parts has been performed. The result of this calculation can explain the feature of the present data at forward angles below 600 MeV and indicates that an additional background amplitude is required for the S wave around 500 MeV.

1. Introduction

The study of the process $\gamma+N\rightarrow\pi+N$ gives us a unique information on the "Baryon Spectroscopy" such as not only the amplitudes of baryon resonances but also their relative signs to the Born term. Photons are also a good probe to study the structure of the nucleon and the nucleon resonances because the electromagnetic interaction can be described exactly the quantum electrodynamics. From this reason, the pion photoproduction processes have been studied for many years both experimentally and theoretically in spite of difficulties of the experiment due to the bremsstrahlung beam with continuous energy spectrum and the complexity of the amplitude analysis due to spin 1 of a photon.

The amplitudes of photoproduction processes can be expressed as

$$A^{+}=A(\gamma+p\rightarrow\pi^{+}n)=-\sqrt{\frac{1}{3}}A^{V3}+\sqrt{\frac{2}{3}}(A^{V1}-A^{S}) \tag{1-1}$$

$$A^{\circ}=A(\gamma+p\rightarrow\pi^{\circ}+p)=\sqrt{\frac{2}{3}}A^{V3}+\sqrt{\frac{1}{3}}(A^{V1}-A^{S}) \tag{1-2}$$

* Now at Institute for Nuclear Study, University of Tokyo, Tanashi, Tokyo.

$$A^- = A(\gamma + n \to \pi^- + p) = \sqrt{\frac{1}{3}}\, A^{V3} - \sqrt{\frac{2}{3}}\,(A^{V1} + A^S) \qquad (1\text{–}3)$$

$$A^{n^\circ} = A(\gamma + n \to \pi^\circ + n) = \sqrt{\frac{2}{3}}\, A^{V3} + \sqrt{\frac{1}{3}}\,(A^{V1} + A^S), \qquad (1\text{–}4)$$

where A^S represents the isoscalar amplitude which leads to I=1/2 final states, and A^{V3} and A^{V1} are the isovector amplitudes which leads to I=3/2 and 1/2 final states, respectively. In the process $\gamma+p\to\pi^\circ+p$, the pion exchange term does not contribute and the electric Born term is much smaller than in the process $\gamma+p\to\pi^++n$ at forward angles. The amplitude of the process $\gamma+p\to\pi^\circ+p$ is mostly attributed to the resonance amplitude at forward angles. Then the precise measurement of the process $\gamma+p\to\pi^\circ+p$ is very useful to study the resonance amplitudes in detail.

Photon couplings of a proton target for large resonances such as $P_{33}(1232)$, $D_{13}(1510)$ and $F_{15}(1650)$ resonances are considered to be well established, although the recent energy independent analysis by Berends and Donnachie[1] gives a rather different values for the photon couplings of the $D_{13}(1510)$ resonance. There are some ambiguities in the photon couplings of small resonances such as $S_{11}(1530)$, $S_{31}(1660)$, $S_{11}(1700)$ and $P_{11}(1650)$. These couplings given by various phenomenological analyses[2~8] are listed in Table 1. In the energy region around 750 MeV, it is well known that the $D_{13}(1510)$ resonance amplitude with helicity $\frac{3}{2}$ (B_{2-}) dominates. (The helicity $\frac{1}{2}$ amplitude of the $D_{13}(1510)$ resonance (A_{2-}) is known to be quite small.) This helicity $\frac{3}{2}$ amplitude goes down to zero at 0° and 180° from the conservation of angular momentum. Then the data at forward angles below 750 MeV are sensitive to the small resonances of S and P waves.

Table 1. Photon couplings of small resonances for the process $\gamma+p\to\pi^++n$. $(\mu b)^{1/2}$

Resonance	MW[2]	MOR[3]	F[4]	DLR[5]	C[6]	BC[7]	BCP[8]
S_{11} (1510)	63±13	36± 2	70± 4	78±20	82± 7	63	75
S_{31} (1660)	105±38	78± 6	−5±16	−10±17	44±27	55	40
S_{11} (1700)	12±15	54± 5	68± 9	29±18	44±18	44	50
P_{11} (1650)	−68±24	16±25	53±19	−14±21	62± 7	5	−2

There have been many cross section measurements with high statistics compared with polarization measurements, but there are still discrepancies among the data of the cross section for the process $\gamma+p\to\pi^\circ+p$ in the energy region from 400 MeV to the second resonance ($D_{13}(1510)$) region. Therefore, the differential cross sections of the process $\gamma+p\to\pi^\circ+p$ were measured with an increased accuracy in the energy region between 450 MeV and 975 MeV. The measurement has been performed in the angular region from 15° to 130° of the pion CM angle θ_π^* by two different systems with the same beam and target to reduce the systematic error. At forward angles, the recoiled proton from the process $\gamma+p\to\pi^\circ+p$ has an extremely low momentum and is unable to be detected due to the large multiple Coulomb scattering and energy losses in the target material and detecting devices. Therefore, two photons decayed from a π° meson were detected with "π°-system" at angles of 15°, 35° and 50°. In the angular region of θ_π^* from 50° to 130°, the recoiled proton was detected in coincidence with one of photons decayed from a π° meson (called as "γ–p system"). The

"γ–p system" is described in detail elsewhere.[9] Overlapping of data by the two systems was made at $\theta_\pi^* = 50°$ around 675 MeV.

2. Experimental Procedure

2–1. Experimental Layout

The bremsstrahlung beam produced from the 1.3 GeV electron synchrotron at the Institute for Nuclear Study, University of Tokyo, was incident on a liquid hydrogen target. The experimental layout is shown in Fig. 1.

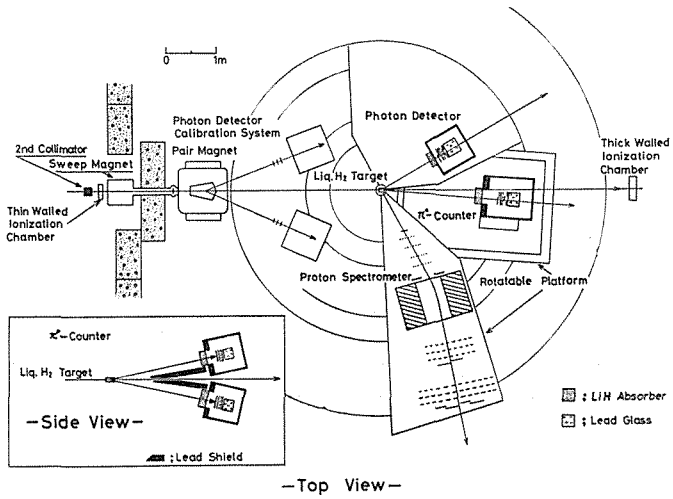

Fig. 1. Experimental layout.

In the "π°-system", the energies and the correlation angle of two photons decayed from a π° meson were measured by two photon detectors. The system was mounted on a rotatable platform. The two photon detectors were set symmetrically up and down with respect to the horizontal plane. The angle subtended by two photon detectors was carefully adjusted corresponding to the energies of the incident photon. In order to maintain maximum efficiency in detecting two photons from a π° meson, the opening angle of photon detectors was chosen to be the minimum correlation angle $\phi_{\min}$ defined by the relation;

$$\sin\left(\frac{\phi_{\min}}{2}\right) = \frac{\mu_\pi}{E_\pi}, \tag{2–1}$$

where μ_π and E_π were the rest mass and energy of the π° meson, respectively. The photon detectors were exposed with rather heavy backgrounds due to the electromagnetic processes around the target, because the photon detectors were set close to the beam line. Therefore, a collimator made of lead of 10 cm in thickness was set in front of each photon detector to reduce the background. The flight path of photons was also carefully shielded from the beam line with lead blocks except around the target area.

2–2. Beam and Target

The bremsstrahlung beam was produced from a platinum radiator of 50 μm in thickness irradiated with electrons accelerated up to the desired energy in the synchrotron. The beam was collimated by a lead collimator of 5 mm in diameter placed at 2.4 m apart from the radiator. A halo of the beam was cut by the second lead collimator of 12 mm in diameter placed at 4.3 m downstream from the first one. At the target point where was 16 m downstream from the radiator, the beam profile was a circle with a diameter of 22 mm. Two magnets were set behind each collimator and swept out charged particles in the beam. A vacuum duct was installed along the beam path to reduce electrons and/or positrons produced in the air.

The absolute intensity of the exposed photons was monitored by a thick walled ionization chamber, which was calibrated by a Faraday cap using an extracted electron beam. A thin walled ionization chamber was also used as an auxiliary beam monitoring system. The average intensity during the experimental run ranged from 0.8 to 1.5 times 10^9 equivalent quanta per second. The beam condition was monitored by an event rate of a threefold coincidence of scintillation counters which were placed behind the pair magnet shown in Fig. 1. No appreciable variation was found beyond statistical fluctuations throughout the present experiment.

Liquid hydrogen was contained in a container of 40.6 mm in diameter and 106.5 mm long, which was made of Mylar of 75 μm in thickness at both end caps and 125 μm in thickness at side wall. The container was installed in a vacuum vessel to reduce the thermal heat radiation. The thickness of the Mylar window of the vessel was 250 μm. The arrangement of the beam line and the target is shown in Fig. 2.

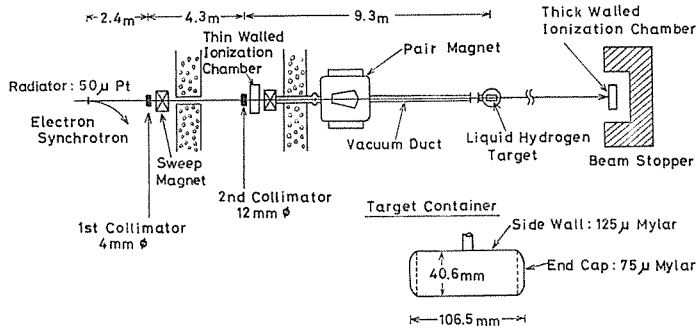

Fig. 2. Arrangement of the beam line and the target.

2–3. π°-counter

A π° meson decays into two photons instantly. The π°-counter consisted of two photon detectors which measured the energies and flight directions of two decayed photons. A schematic diagram of the π°-counter is given in Fig. 3. Each photon detector consisted of the following five components;

1) a lead glass Cherenkov counter of total absorption type made of SF–2 flint glass with a dimension of 25 cm (8.8 radiation lengths) cubic and viewed by 16 RCA 6655A photomultipliers with an optical contact of a silicon rubber,

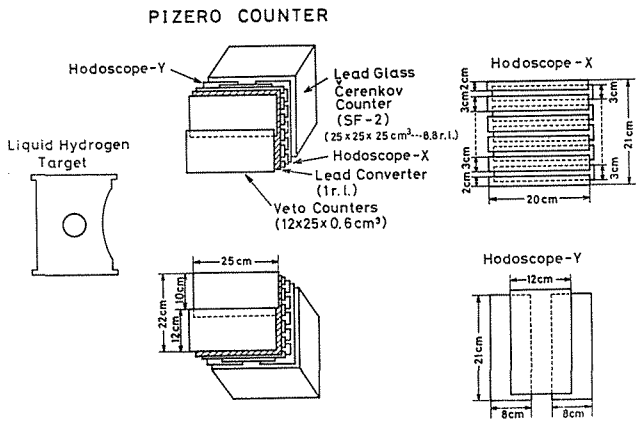

Fig. 3. Schematic diagram of the π°-counter.

2) arrays of hodoscope scintillation counters viewed by 11 XP 1110 photomultipliers (vertical direction counters denoted as Hodoscope X) and 3 RCA 6655A photomultipliers (horizontal direction counters denoted as Hodoscope Y) through an optical contact with an acrylite pipe and a silicon rubber,
3) a lead plate converter of 5 mm thick in which about half of photons is converted to electron and positron pairs,
4) veto scintillation counters to reject charged particles viewed by 2 RCA 6655A photomultipliers with the same optical contacts as the hodoscope counters

and 5) a LiH absorber of 10 cm or 20 cm thick depending on the set up to absorb low energy photons.

The sizes of these counters are listed in Table 2. The energies of photons were measured by the pulse heights from the Cherenkov counters. Assuming that π° mesons were produced at the center of the target, the flight directions of photons, which were converted to electron and/or positron were measured from the bit patterns of hodoscope counters. The spacial resolutions of hodoscope counters were 10 mm and 40 mm for X and Y directions, respectively.

Table 2. Dimensions of counters.

Counter		Dimension (mm³)
Hodoscope X	End Counters	20×200×6
	Others	30×200×6
Hodoscope Y	End Counters	80×210×6
	Center Counter	120×210×6
Veto Counters		120×250×6

The kinematical values of the detected π° meson were calculated from the relations;

$$E_{\pi}=k_1+k_2 \tag{2-2}$$

$$\vec{P}_{\pi}=\vec{k}_1+\vec{k}_2 \tag{2-3}$$

$$\mu_{\pi}{}^2=2k_1k_2(1-\cos\phi), \tag{2-4}$$

where E_π, $\vec{P}_\pi$, μ_π, ϕ, $\vec{k}_1$ and $\vec{k}_2$ are the energy, momentum, rest mass of a π° meson, the correlation angle of decayed two photons and their momenta, respectively. k_1 and k_2 are the energies of the two photons. $\vec{k}_1$, $\vec{k}_2$, k_1, k_2 and ϕ can be obtained from the pulse heights of the Cherenkov counters and the bit pattern of the hodoscope counters.

The energy response of the Cherenkov counters was measured by the monoenergetic electron beam analysed by a pair magnetic spectrometer system shown in Fig. 1. The energy response of the Cherenkov counter is shown in Fig. 4. The pulse height spectra were fitted with the Gaussian form to evaluate the energy resolutions of the Cherenkov counters. The fractional resolution is shown in Fig. 5 and can be approximated by

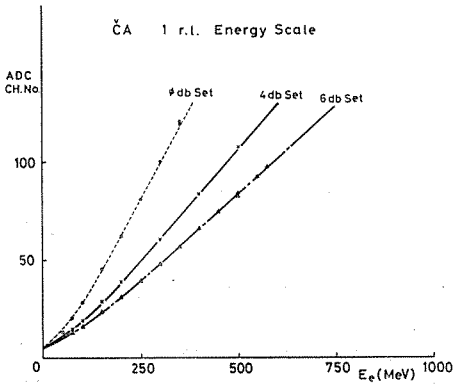

Fig. 4. Energy response of the Cherenkov counter.

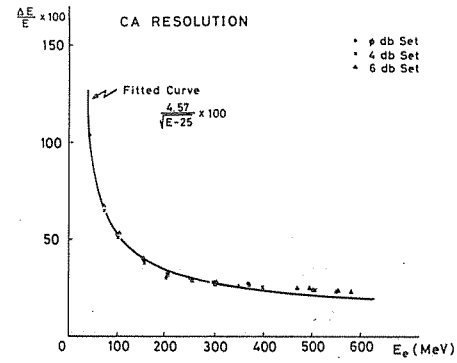

Fig. 5. Energy resolution of the Cherenkov counter.

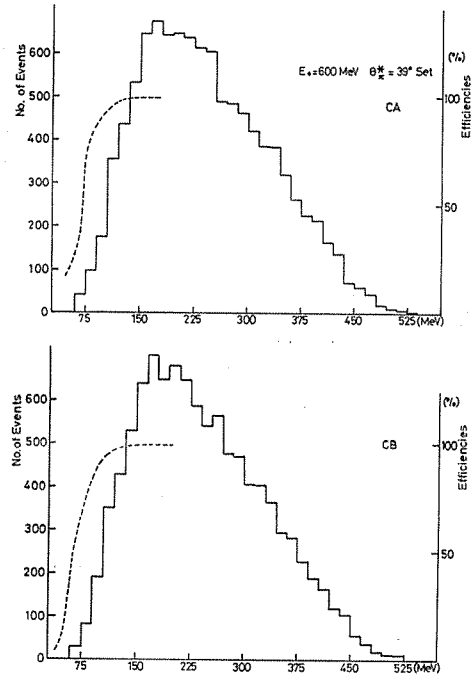

Fig. 6. Energy distributions of acceptable photons (histgram) and the efficiency of the Cherenkov counters (dashed lines) in the case of E_0=600 MeV and θ_π^*=39° set.

$$\frac{\Delta E}{E} = \frac{C}{\sqrt{E-25}}, \tag{2-5}$$

where E and ΔE are the incident energy and FWHM of the pulse height spectra, respectively. The values of C are 4.57 and 4.54 for two photon counters when E is given in MeV.

The discrimination levels of the Cherenkov counters were set to be low enough comparing with the energies of accepted photons as are illustrated in Fig. 6 and are listed in Table 3. The variation of the discrimination level throughout the run was less than 2 MeV and gave no effect on the detection efficiency of the Cherenkov counters.

Table 3. Discrimination levels of Cherenkov counters.

Experimental Run		Discrimination Level (MeV)	
E_0 (MeV)	θ_π^* (DEG)	CA	CB
850	50	53.3	55.0
600	15	43.1	42.4
700	15	43.1	42.4
850	15	53.3	55.0
600	39	43.1	42.4
700	35	43.1	42.4
850	35	53.3	55.0
1000	37	53.3	55.0

The symbols E_0 and θ_π^* denote the top energy of the bremsstrahlung and the pion CM angle, respectively.

2–4. Data Taking and Monitoring System

The block diagram of electronic circuits is shown in Fig. 7. Following notations are used hereafter,

CA (CB); a signal from the Cherenkov counter
HAX (HBX); signals from Hodoscope X counters
HAY (HBY); signals from Hodoscope Y counters
VA (VB); a signal from the veto counter,

where A and B denote the photon detectors which are set up and down with respect to the horizontal plane, respectively. A threefold coincidence signal of CA (CB), HAX (HBX) and HAY (HBY) with a time resolution of 20 nsec is represented as $CA \cdot HAX \cdot HAY$ ($CB \cdot HBX \cdot HBY$). The signal of $CA \cdot HAX \cdot HAY \cdot \overline{VA}$ ($CB \cdot HBX \cdot HBY \cdot \overline{VB}$) is defined as a gamma signal γA (γB) where $\overline{VA}$ ($\overline{VB}$) denotes an anti-coincidence. The time resolution of the anti-coincidence was 20 nsec. A coincidence signal between two gamma signals γA and γB with a time resolution of 30 nsec was defined as "π°" signals. Coincidence signals $CA \cdot HAX \cdot HAY \cdot VA$ ($CB \cdot HBX \cdot HBY \cdot VB$) were considered as charged particle signals. The coincidence of two charged particle signals with a time resolution of 30 nsec produced "charged coincidence ($C.C.$)" signals. The "charged coincidence" events were recorded to monitor the electromagnetic background. Light pulsers made of light emission diodes which were mounted on the front faces of lead glass Cherenkov counters were

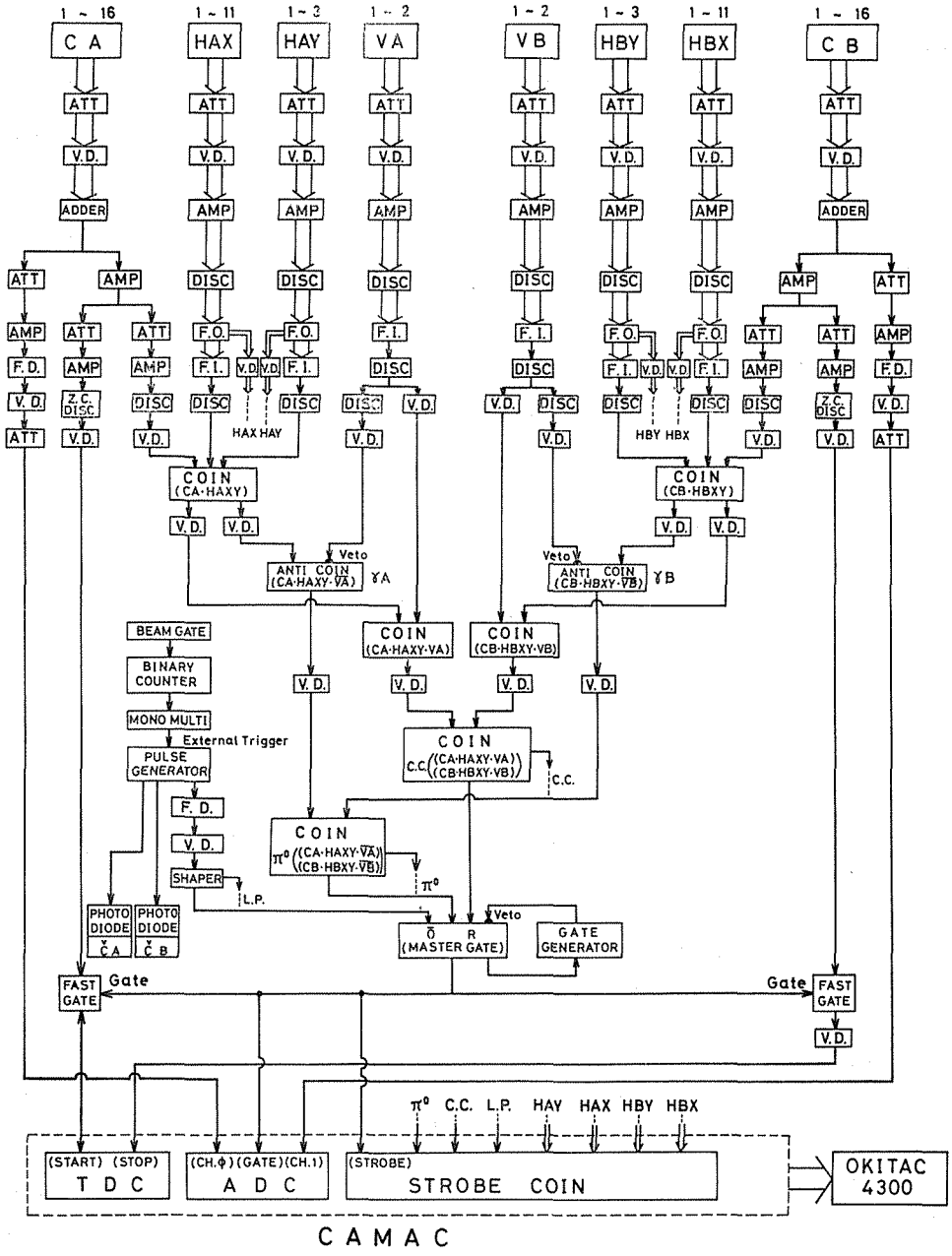

Fig. 7. Block diagram of electronic circuits. The notations are: ATT, attenuator; V. D., variable delay; AMP, fast amplifier; DISC, discriminator; F. D., fixed delay; F. O., fan-out; F. I., fan-in; ZCDISC, zero cross discriminator; COIN, coincidence; ANTI COIN, anti-coincidence; OR, or-circuit; STROBE COIN, strobed coincidence; TDC, time-to-digital converter; ADC, analogue-to-digital converter. In this diagram, circuits for delayed coincidences are omitted.

fired at the beam off time to monitor the gain of the Cherenkov counters. These signals were also recorded as "*L.P.*" signals. A master gate signal (*M.G.*) was generated for any one of "π°" signals, "*C.C.*" signals and "*L.P.*" signals and could be written logically by

$$\begin{aligned}(M.G.)&=\text{“}\pi^{\circ}\text{”}+\text{“}C.C.\text{”}+\text{“}L.P.\text{”}\\&=(CA\cdot HAX\cdot HAY\cdot \overline{VA})\cdot(CB\cdot HBX\cdot HBY\cdot \overline{VB})\\&\quad+(CA\cdot HAX\cdot HAY\cdot VA)\cdot(CB\cdot HBX\cdot HBY\cdot VB)+\text{“}L.P.\text{”}.\end{aligned}\tag{2-6}$$

The *M.G.* signal was used to interrupt a computer and gate the ADC circuits, strobed coincidence circuits and "Fast Gate" circuits. The "Fast Gate" circuits were used to reduce accidental events in the measurement of the time difference between *CA* and *CB* signals. The durations of gate pulses for the ADC, the "Fast Gate" circuits and the strobed coincidence circuits were 40, 40 and 25 nsec, respectively.

The data were stored at first in the OKITAC 4300 minicomputer through a camac interface. The block diagram of the data taking system is shown schematically in Fig. 8. All CAMAC modules were inhibited in 1.2 msec after each interruption. The following informations for each event were stored in the computer; (1) kinds of the master gate, (2) bit pattern of hodoscope counters, (3) pulse heights of the Cherenkov counters and (4) the time difference between *CA* and *CB* signals. The stored format in the OKITAC 4300 are shown in Fig. 9. The performances of detectors for each run were monitored with the following distributions;

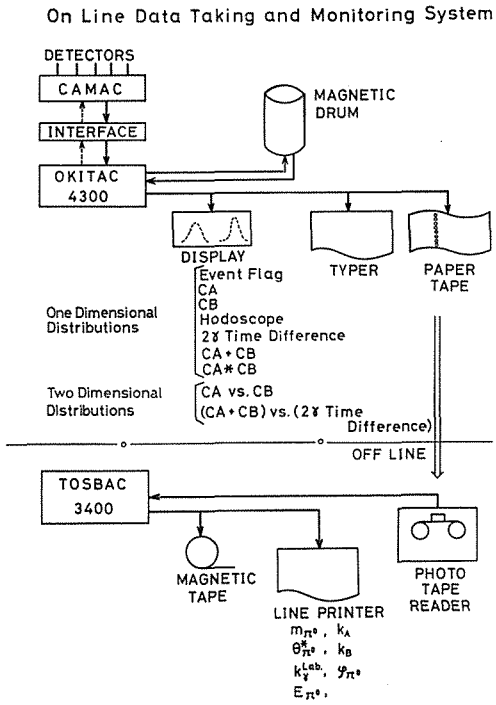

Fig. 8. Block diagram of the data taking system.

0									15
π°	b	C.C.	b	L.P.	b	b	b	Time Difference	
CA Pulse Height								CB Pulse Height	
b	HAY		b					HAX	
b	HBY		b					HBX	

Fig. 9. Data format of the π°-system.

(I) one dimensional distributions
event number of "π°", "*C.C.*" and "*L.P.*",
(2) fired hodoscope distributions,
(3) distributions of analogue signals such as CA, CB, $CA+CB$ and $CA\times CB$, which corresponded roughly to k_1, k_2, E_π and $\frac{\mu_\pi{}^2}{2(1-\cos\phi)}$ respectively.
(4) distribution of the time difference between CA and CB

and

(II) two dimensional distributions
(1) CA vs. CB
(2) $(CA+CB)$ vs. time difference between CA and CB signals.

The spill time of the photon beam has been kept constant about 4~5 msec to minimize the variation of accidental events. Events of delayed coincidence between $CA\cdot HAX\cdot HAY$ ($CB\cdot HBX\cdot HBY$) and VA (VB) were also recorded throughout each experimental run. The rate of over killing by the veto counters was estimated with this delayed coincidence rate and amounted to 5.4% at the run of $\theta_\pi{}^*=15^\circ$ and 1.3% at the run of $\theta_\pi{}^*=50^\circ$.

Table 4. Set up parameters and resolutions of the π°-counter.

Experimental Run	Set Up Parameters				Resolutions				
E_0 (MeV)	$\theta_\pi{}^*$ (DEG)	L (mm)	κ (DEG)	ε (DEG)	Δk_γ (MeV)	$\Delta\theta_\pi{}^*$ (DEG)	ΔE_π (MeV)	$\Delta\mu_\pi$ (MeV)	$\Delta k_1(\Delta k_2)$ (MeV)
850	50	2006.3	31.8	12.25	30	2.2	30	25	50
600	15	1937.9	10.3	17.25	25	2.2	25	30	45
700	15	2262.7	9.2	14.50	30	1.6	30	30	45
850	15	2262.7	9.2	11.25	30	1.4	35	25	50
600	39	1929.9	26.4	17.25	25	2.2	25	30	40
700	35	2273.7	21.8	14.50	25	1.6	25	30	40
850	35	2272.8	21.8	11.75	30	1.6	30	25	50
1000	37	2272.2	21.8	9.75	40	1.6	40	20	50

The notations are; E_0, top energy of the bremsstrahlung; $\theta_\pi{}^*$, pion CM angle; k_γ, energy of the incident photon; E_π, energy of pion in the laboratory system; μ_π, measured value of pion mass; k_1 (k_2), energy of the decayed photon from a π° meson. L, κ, ε are illustrated in Fig. 10.

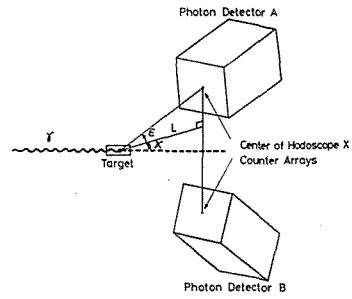

Fig. 10. Notations of set up parameters.

The data have been taken with three angles of 15°, 35° and 50° in the pion CM angles and with the combination of four maximum photon energies of 600, 700, 850 and 1000 MeV. These combinations are listed in Table 4. The notations of set up parameters are shown in Fig. 10.

3. Data Analysis and Reduction of the Cross Section

3–1. Events Selection

The measured events were selected with the following steps.

(1) Events which fired more than 3 (2) adjacent hodoscope X (Y) counters or more than two counters apart from each other were called as "Hodoscope OUT" events and were rejected. The events which passed this criterion in both hodoscopes were named "Hodoscope OK" events.

(2) The example of the distribution of the time difference between CA and CB signals is shown in Fig. 11. A clear peak corresponding to π° events is seen. Events which fall outside the peak area were rejected.

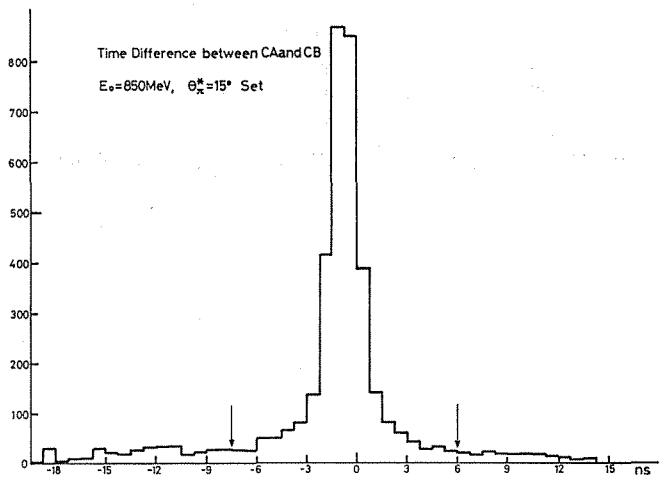

Fig. 11. Distribution of time difference between CA and CB. Arrows indicate the region of selection.

(3) Events whose measured quantities did not satisfy the kinematics of the process $\gamma+\mathrm{p}\rightarrow\pi^\circ+\mathrm{p}$ were rejected. This criterion was realized with the following relation;

$$|\cos\theta_\pi^*| = \left| \frac{E_\pi^* - \frac{k_\gamma}{k_\gamma^*}(E_\pi - P_\pi\cos\theta_\pi)}{P_\pi^*} \right| > 1\,, \qquad (3\text{–}1)$$

where E_π, P_π, θ_π and k_γ were the energy, momentum and the production angle of the π° meson and the responsible incident photon energy in the laboratory system, respectively. The symbols with an asterisk represent corresponding quantities in the CM system. The left hand side of (3–1) represents $|\cos\theta_\pi^*|$ if the particle is assumed to be produced at the center of the target by the process $\gamma+\mathrm{p}\rightarrow\pi^\circ+\mathrm{p}$. In this equation,

all kinematical values are calculated from the measured energies and emission angles of two photons.

(4) Events whose values of k_1, k_2 or k_1+k_2 were outside the distributions of the corresponding values calculated by Monte Carlo method were rejected. (The events rejected by this criterion were scarce.)

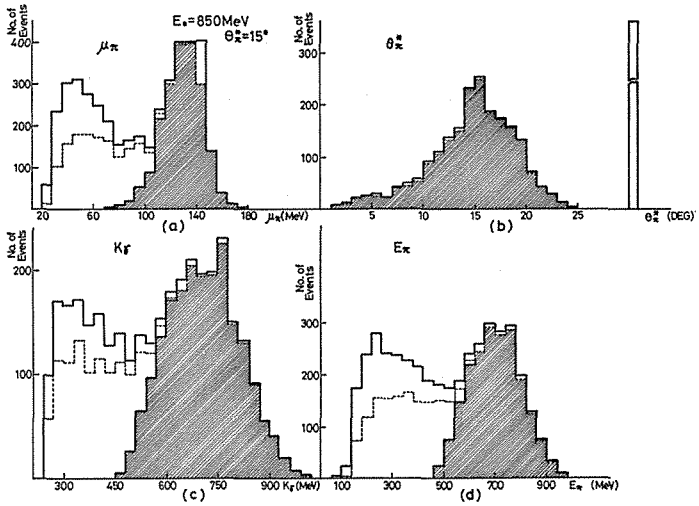

Fig. 12. (a) Distribution of the mass of the π° meson evaluated from the measured momenta of two photons.
(b) Distribution of the pion CM angle.
(c) Distribution of the responsible incident photon energy in Lab. system.
(d) Distribution of the pion energy in Lab. system. Solid, dashed and shaded histgrams represent the distributions of all "Hodoscope OK" events, events between two arrows in Fig. 11 and events which are not rejected by the relation (3–1), respectively.

The various distributions for the "Hodoscope OK" events are illustrated in Fig. 12(a)$\sim$12(d), where solid line, dashed line and shaded area represent the total "Hodoscope OK" events, the events in the peak area of the time difference distribution between *CA* and *CB* and the selected events with the relation (3–1), respectively.

"Hodoscope OUT" events rejected at the step (1) were caused by the accidental firing of the hodoscope counters in addition to the two photons from a π° meson. Therefore, the same portion of "Hodoscope OUT" events should be included in the selected events as the portion of "Hodoscope OK" events which passed all selection criteria. This correction factor amounted to from 1.10 to 1.19 depending on the runs.

In the present experiment, the events which occurred in the Mylar wall of the container of the liquid hydrogen were also included. At the measurement for $\theta_\pi^* = 15^\circ$, the π°-counter also detected the events occurred in the Mylar window of the vacuum vessel. These events were subtracted statistically by executing empty target runs.

The rate of the accidental coincidence between γA and γB was estimated from the event rate outside the peak area of the time difference distribution. This correction was estimated to be 2.4% at most.

3–2. Reconstruction of the Selected Events

The energy resolution of the Cherenkov counter was relatively poor. Then the energies of two photons decayed from a π° meson were reevaluated by the modified Tau's method.[10,11] The essential point of the modification was the usage of the energy dependence of the resolution of the Cherenkov counters on the constraint condition to find the most probable energies of two photons using the constraint between the correlation angle and the energies of two photons from a π° meson.

The reaction point of each event was assumed to be the center of the liquid hydrogen target in this reconstruction procedure.

3–3. Monte Carlo Calculation of the Detection Efficiencies

The detection efficiency of the π°-counter was evaluated by the Monte Carlo calculation with the computers TOSBAC 3400 at INS and HITAC 8700 at KEK. The flow chart of the Monte Carlo calculation is shown in Fig. 13. In the calculation the next conditions were taken into account; (1) the energy resolutions of the

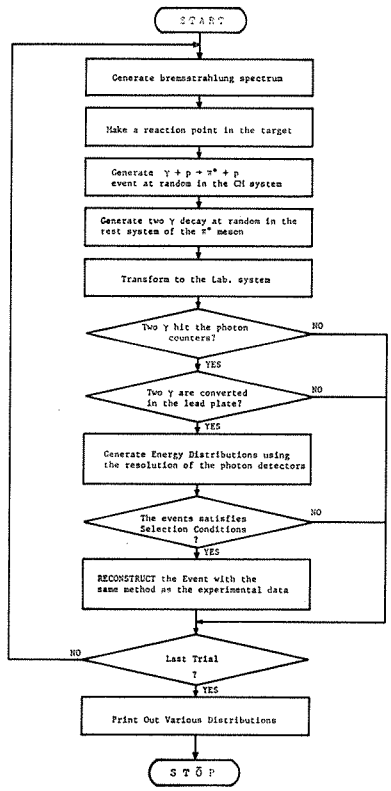

Fig. 13. Flow chart of the Monte Carlo calculation.

Cherenkov counters, (2) the energy loss of a photon in the lead converter, (3) the conversion efficiency of a photon by the lead converter and (4) the distribution of the reaction point in the target. The energy resolution was approximated by the equation (2–5). The energy loss of photons in a lead plate is different from that of electrons as shown in Fig. 14 and was taken into account. The conversion efficiency η_{conv} of the lead converter is calculated by the formula;

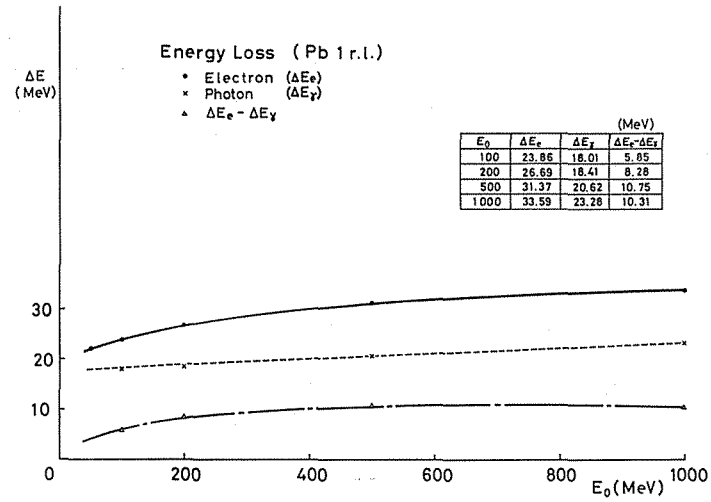

Fig. 14. Energy loss of photons and electrons in a lead plate with the thickness of 1 radiation length.

$$\eta_{conv}=1-\exp(-\mu),$$

with (3–2)

$$\mu=\sigma_{pair}\cdot\rho\cdot N\cdot t/A.$$

Symbols σ_{pair}, ρ, N, t and A are the total cross section of pair creation (cm^2/atom), the density of lead (11.35 g/cm^3), Avogadro's number (6.022×10^{23} $mole^{-1}$), thickness of the lead plate (0.5 cm) and mass number of lead (207.19), respectively. σ_{pair} was calculated by the Hatree-Fock-Slator model with screening.[12] The reaction point was assumed to have a uniform distribution in the direction of the beam line and to have a Gaussian distribution with the standard deviation of 0.8 cm in the direction perpendicular to the beam line. The selection condition of the equation (3–1) was also included in this calculation.

The experimental yield is represented as,

$$Y_E=\int dk\int d\Omega\cdot\frac{d\sigma}{d\Omega^*}\cdot N_T\cdot J\cdot\eta\cdot N_\gamma. \tag{3–3}$$

The total number of the exposed photons N_γ is written as,

$$N_\gamma=\left(\frac{1}{E_0}\int_0^{E_0}kB(k)\,dk\right)N_{M.U.}=\frac{\alpha_I\cdot\alpha_C}{E_0}\cdot N_{M.U.}=Q, \tag{3–4}$$

where E_0 is the top energy of the bremsstrahlung beam, $B(k)$ is the spectrum function in the Schiff's thin target formula,[13] $N_{M.U.}$ is the count number of the current inte-

grator with calibration constant α_I (Coulomb/count). α_C is the calibration constant of the thick walled ionization chamber (MeV/coulomb) and Q is the equivalent quanta irradiated in the experiment. $\frac{d\sigma}{d\Omega^*}$, N_T and J are the differential cross section in the CM system, the number of nucleons in the target and the Jacobian of the transformation from the laboratory system to the CM system, respectively. η is the overall detection efficiency including the conversion efficiency and an attenuation factor η_{LiH} due to the LiH absorber. The yield of the Monte Carlo calculation is expressed as,

$$Y_M = \int dk \int d\Omega \cdot N_G \cdot J \cdot \eta_M / \alpha_G , \tag{3-5}$$

where N_G is the total generated number of photons and is written

$$N_G = \frac{1}{E_0} \int_0^{E_0} kN(k)dk, \tag{3-6}$$

where $N(k)$ is the spectral function of the bremsstrahlung and is related to $B(k)$ with a normalization constant C_0 by

$$N(k) = C_0 \frac{B(k)}{k} . \tag{3-7}$$

The total number of the generated events M_T is written as

$$M_T = \int_{k\min}^{k\max} N(k)dk, \tag{3-8}$$

where $k_{\min}$ and $k_{\max}$ are the minimum and maximum energies of the generated photons, respectively. In this calculation, the emission angle of a π° meson and the decay angle of the π° meson into two photons are limited within appropriate regions to achieve efficient calculations. α_G is a correction factor due to this limitation. The detection efficiency η_M thus calculated is related to the experimental detection efficiency η as,

$$\eta = \eta_M \cdot \eta_{\mathrm{LiH}} , \tag{3-9}$$

because the calculation excluded the attenuation factor due to the LiH absorber. The factor η_{LiH} was 0.745 for the run of $\theta_\pi^* = 15^\circ$ and 0.85 for the other runs. Using the relations (3-3), (3-5), (3-6), (3-7), (3-8) and (3-9), the differential cross section can be written by the formula;

$$\frac{d\sigma}{d\Omega^*} = \frac{Y_E}{Q} \Big/ \left[N_T \cdot \frac{Y_M}{M_T} \cdot \alpha_G \cdot \eta_{\mathrm{LiH}} \cdot f(k_{\min}, k_{\max}, E_0) \right], \tag{3-10}$$

where the function $f(k_{\min}, k_{\max}, E_0)$ represents the following quantity,

$$f(k_{\min}, k_{\max}, E_0) = \frac{\int_{k\min}^{k\max} \frac{B(k)}{k} dk}{\frac{1}{E_0} \int_0^{E_0} B(k)\, dk} \tag{3-11}$$

and is calculated from the Schiff's formula.

The differential cross section was assumed to be constant with respect to the photon energy in the calculation at the first step. After the first reduction of the cross section using the relation (3-10), the iteration was made with the energy de-

pendence of the cross sections obtained at the first step. The results of the first and second steps on the differential cross sections were close enough each other except at the run with the top energy of 600 MeV and the center of mass angle of 39°. The differences between the results of the first step and the second step amounted to between 1.5% and 8.7% for various energy bins of this run. The result of the third step was close enough to the result of the second step for this run and the extracted energy dependence was correct.

The distributions of various quantities obtained from the measured events were in good agreement with those of the Monte Carlo calculation as is shown in Fig. 15.

The resolutions for E_π, P_π, k_γ, θ_π^*, ϕ_π^*, k_1, k_2 and μ_π were evaluated from the Monte Carlo calculation and the results are listed in Table 4 together with the set up parameters of each run.

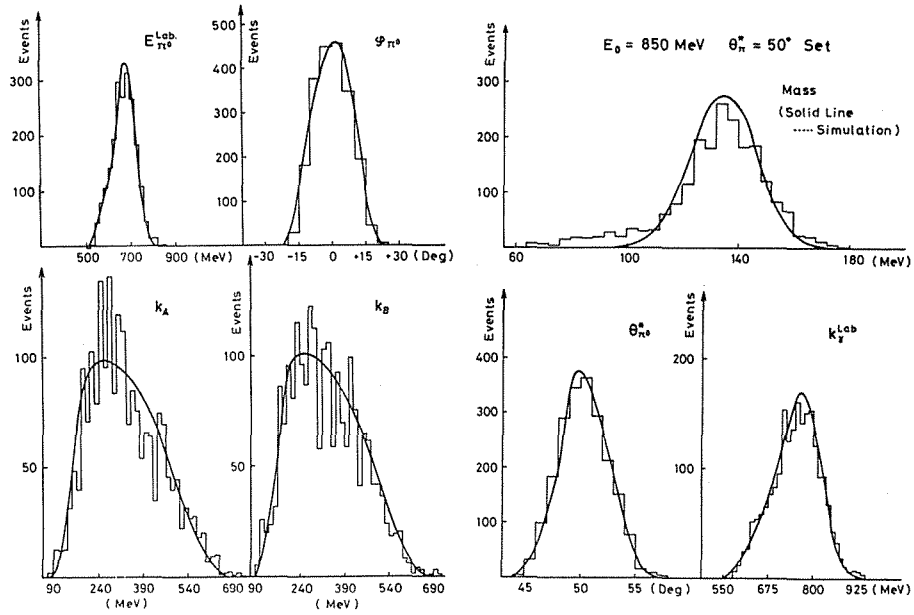

Fig. 15. Comparison of various distributions from experimental yields with those of Monte Carlo calculation for the case of E_0=850 MeV and θ_π^*=50°.

4. Experimental Results and Analysis

4–1. The Differential Cross Sections

The differential cross sections were measured at eight different experimental conditions of the "π^0-system" which are given in Table 4. The data bin was chosen to be 25 MeV which is almost equal to the energy resolution of the incident photon energy for the "π^0-system". The angular acceptance in the CM angle of the data ranged from 2° to 3° at FWHM and the angular resolution of the detection system was somewhat better than the acceptance. The differential cross sections are listed in Table 5 and the typical angular dependences are shown in Fig. 16(a)~(d) together with the results obtained with the "γ–p system". The present measurement and the measurement with the "γ–p system" overlapped at the CM angle of 50° and in the

Table 5. Final result of the cross sections.

Top Energy of Bremsstrahlung	Energy, Bin	Pion CM Angle	Differential Cross Section
E_0 (MeV)	$k_\gamma \pm \Delta k_\gamma$ (MeV)	θ_π^* (DEG)	$\frac{d\sigma}{d\Omega^*} \pm \Delta\left(\frac{d\sigma}{d\Omega^*}\right)$ (μb/sr.)
		15°	
600	450±12.5	14.8	5.753±0.470
	475±12.5	14.9	5.342±0.407
	500±12.5	15.1	4.494±0.357
	525±12.5	15.3	3.441±0.302
	550±12.5	15.5	3.131±0.377
700	550±12.5	13.8	2.948±0.273
	575±12.5	13.9	2.038±0.232
	600±12.5	14.1	1.829±0.214
	625±12.5	14.2	1.497±0.231
	650±12.5	14.4	0.804±0.245
850	650±12.5	14.4	0.917±0.205
	675±12.5	14.5	1.306±0.182
	700±12.5	14.7	1.180±0.123
	725±12.5	14.9	1.353±0.126
	750±12.5	15.0	1.302±0.124
	775±12.5	15.1	0.979±0.117
	800±12.5	15.3	0.791±0.113
	825±12.5	15.4	0.918±0.132
		35°	
600	450±12.5	37.2	6.862±0.484
	475±12.5	37.6	5.263±0.312
	500±12.5	38.1	4.537±0.245
	525±12.5	38.5	3.409±0.215
	550±12.5	38.9	2.776±0.212
	575±12.5	39.3	2.313±0.229
700	575±12.5	32.6	2.066±0.159
	600±12.5	33.0	1.550±0.165
	625±12.5	33.3	1.660±0.154
	650±12.5	33.6	1.205±0.181
	675±12.5	34.0	1.209±0.253
850	675±12.5	34.0	1.568±0.214
	700±12.5	34.3	1.747±0.144
	725±12.5	34.6	1.826±0.151
	750±12.5	35.0	2.097±0.152
	775±12.5	35.3	1.966±0.119
	800±12.5	35.6	2.151±0.140
	825±12.5	35.9	1.926±0.156
1000	825±12.5	35.9	1.949±0.137
	850±12.5	36.2	1.434±0.130
	875±12.5	36.5	1.380±0.092
	900±12.5	36.8	1.238±0.104
	925±12.5	37.1	1.167±0.107
	950±12.5	37.4	1.302±0.113
	975±12.5	37.7	1.487±0.130
		50°	
850	675±12.5	48.6	1.700±0.177
	700±12.5	49.1	1.837±0.174
	725±12.5	49.5	2.636±0.192
	750±12.5	50.0	2.800±0.189
	775±12.5	50.4	2.826±0.198
	800±12.5	50.8	2.841±0.205
	825±12.5	51.2	2.657±0.234

The errors quoted in this table include only the statistical ones.

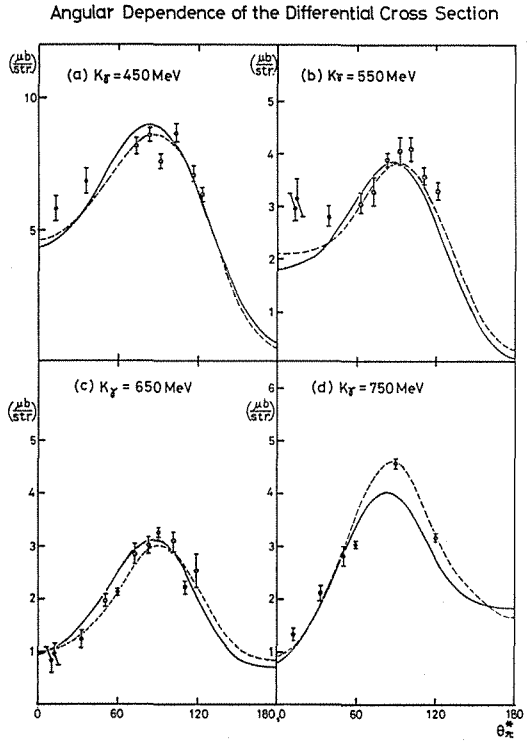

Fig. 16. Angular dependence of the differential cross section at the incident photon energies of (a) 450 MeV, (b) 550 MeV, (c) 650 MeV and (d) 750 MeV. In the figure, black circles represent the data measured with the "π^0-system" and open circles represent the data measured with the "γ-p system". Soild and dashed curves represent the predictions by MOR and MW, respectively.

energy region around 675 MeV. Both results are in good agreement as shown in Fig. 17(c) and then the systematic errors inherent in the individual detection systems are considered to be small. The energy dependence of the cross sections is shown in Fig. 17(a)~(c). The present data at $\theta_\pi^* = 15°$ and 35° are consistent with those of Y. Hemmi et al.[14] at the energies below the second resonance region, but some discrepancies are seen around 950 MeV. At the angle of 50°, the present results are consistent with the data by P. Dougan et al.[15] and by H. De Staebler et al.[16] in the second resonance region.

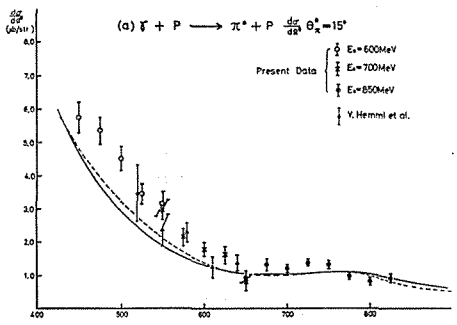

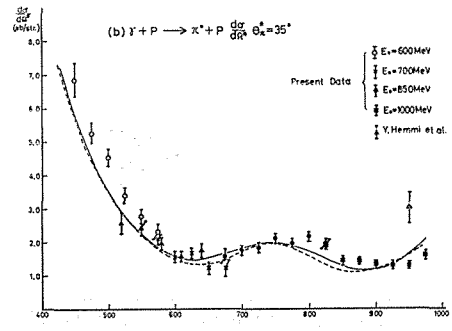

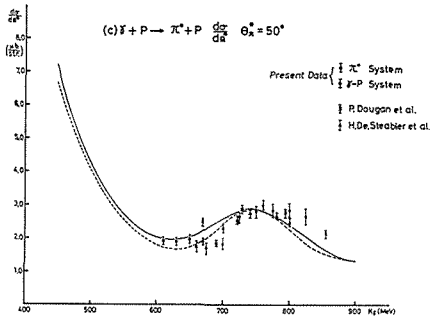

Fig. 17. Energy dependence of the differential cross section at the pion CM angles of (a) 15°, (b) 35° and (c) 50°. Solid and dashed curves represent the predictions by MOR and MW, respectively.

4-2. Errors

Among the errors in the experimental results, the following ones are dependent on experimental set-ups.

(1) Statistical errors due to the experimental and Monte Carlo yields.
(2) Errors in evaluating the over killing ratio due to the high counting rate of the veto counters.
(3) Errors in correction of "Hodoscope Out" events.

The errors presented in Table 5, and Figs. 16 and 17 include only the first one. The others are small and are given in Table 6. In the case of energy bins lower than 150 MeV from the top energy of the bremsstrahlung beam, the background due to the process of double pion production is anticipated. This background was estimated to be less than 5% by a Monte Carlo calculation. The background due to double pion production were also experimentally reduced from the measurement with the different top energies of the bremsstrahlung and was found to be as small as the results by the Monte Carlo calculation. Errors common to all runs are as follows.

Table 6. Errors of various experimental runs.

Experimental Run		Errors in Random Veto Correction	Errors in Hodoscope Out Events Correction
E_0 (MeV)	θ_π^*	(%)	(%)
850	49	0.12	0.81
1000	37	0.42	0.59
850	35	0.15	0.76
700	35	0.80	0.78
600	39	1.13	0.68
850	15	1.12	1.17
700	15	1.15	1.07
600	15	1.12	0.74

The symbols E_0 and θ_π^* denote the top energy of the bremsstrahlung and the pion CM angle, respectively.

(1) Uncertainty of the total photon intensity. (2~3%)
(2) Uncertainty of the number of nucleons in the target container. (1%)
(3) Error in the conversion efficiency of a lead plate. (3.4%)
(4) Error in the attenuation rate of photons in LiH absorber. (1.54% for the run at $\theta_\pi^* = 15°$ and 0.64% for other runs.)

(5) Error due to conversions of decayed photons in liquid hydrogen target. (0.14%)
(6) Uncertainty of the geometrical solid angles of the hodoscope of the photon detectors. (2.3%)

The root of the quadratic sum of these errors amounted to 5.41% for the run at $\theta_\pi^* = 15°$ and 5.22% for the other runs.

4–3. Fixed-t Dispersion Relation Analysis and Discussion

As shown in Figs. 16 and 17, the present data are in good agreement with the analyses by Metcalf and Walker[2] (MW), and Moorhouse, Oberlack and Rosenfeld[3] (MOR), except at the forward angles of 15° and 35° below 600 MeV. The present data are higher than these analyses in this energy and angular region. The analysis by MW is rather phenomenological one in which the amplitudes are decomposed into the Born terms, resonance terms and additional background amplitudes. On the other hand, the analysis by MOR is based on the dispersion relation using K matrix formalism. In order to reduce the discrepancies between the present data and the results of these analyses, the modification on the amplitudes which is sensitive to the cross section at forward angles in this energy region must be required. The helicity 1/2 amplitudes are known to be sensitive to the cross section at forward angles. Therefore in this low energy region, the behaviour of the helicity 1/2 amplitudes of the S and P waves is the subject of present interest.

A simple calculation based on the fixed-t dispersion relation with the resonance saturation of the imaginary parts was executed to study the above problems. At first, each partial wave is assumed to be given by a Breit-Wigner form obtained by R. L. Walker[17] and written as

$$A(W) = A(W_0)\left(\frac{k_0 q_0}{kq}\right)^{1/2} \cdot \frac{W_0 \Gamma^{1/2} \Gamma_\gamma{}^{1/2}}{s_0 - s - i W_0 \Gamma}, \tag{4-1}$$

where

$$\left.\begin{aligned} \Gamma &= \Gamma_0 \left(\frac{q}{q_0}\right)^{2l+1} \cdot \left(\frac{q_0{}^2 + X^2}{q^2 + X^2}\right)^l, \\ \Gamma_\gamma &= \Gamma_0 \left(\frac{k}{k_0}\right)^{2j_\gamma} \cdot \left(\frac{k_0{}^2 + X^2}{k^2 + X^2}\right)^{j_\gamma} \end{aligned}\right\} \tag{4-2}$$

where W_0 and Γ_0 are the mass and width of the resonance, respectively. The symbols k and q are the momenta of the incident photon and produced pion in the CM system, respectively. The symbol s is a usual mandelstam variable and s_0, k_0 and q_0 are the values for corresponding variables at the resonance. The imaginary part of each partial wave is written by,

$$\text{Im } A_{l\pm}(s) = A_{l\pm}(s_0)\left(\frac{k_0 q_0}{kq}\right)^{1/2} \cdot \frac{s_0 \Gamma^{3/2} \cdot \Gamma_\gamma{}^{1/2}}{(s_0 - s)^2 + s_0 \Gamma^2}, \tag{4-3}$$

where $A_{l\pm}(s_0)$ is a photon coupling of each nucleon resonance. The same relation can be written for helicity 3/2 amplitude $B_{l\pm}$ using the photon coupling $B_{l\pm}(s_0)$. From these partial wave amplitudes, the CGLN amplitudes are calculated by the relations;

$$\left.\begin{aligned}
\mathfrak{F}_1 &= \Sigma(P'_{l+1}A_{l+} + P'_l A_{(l+1)-}) + \frac{1}{2}\Sigma[-lP'_{l+1}B_{l+} + (l+2)P'_l B_{(l+1)-}] \\
\mathfrak{F}_2 &= \Sigma(P'_l A_{l+} + P'_{l+1}A_{(l+1)-}) + \frac{1}{2}\Sigma[-(l+2)P'_l B_{l+} + lP'_{l+1}B_{(l+1)-}] \\
\mathfrak{F}_3 &= \Sigma(P''_{l+1}B_{l+} + P''_l B_{(l+1)-}) \\
\mathfrak{F}_4 &= -\Sigma[P''_l B_{l+} + P''_{l+1}B_{(l+1)-}],
\end{aligned}\right\} \tag{4-4}$$

where P_l is the Legendre polynomial. These amplitudes are transformed to the invariant amplitudes by the following relations;

$$F_i = \chi_i^{-1}\mathfrak{F}_i (i=1, \ldots, 4), \tag{4-5}$$

where

$$\left.\begin{aligned}
\chi_1 &= \frac{(W-M)}{8\pi W}\sqrt{(E_1+M)(E_2+M)} \\
\chi_2 &= \frac{(W+M)}{8\pi W}\sqrt{(E_1-M)(E_2-M)} \\
\chi_3 &= \chi_2(E_2+M) \\
\chi_4 &= \chi_1(E_2-M)\,.
\end{aligned}\right\} \tag{4-6}$$

Then, the invariant amplitudes can be expressed as follows;

$$\left.\begin{aligned}
A_1 &= \frac{1}{2W}\left[(W+M)F_1 - (W-M)F_2 - M(\mu^2-t)\left(\frac{F_3}{W-M} + \frac{F_4}{W+M}\right)\right] \\
A_2 &= \frac{1}{2W}[F_3 - F_4] \\
A_3 &= \frac{1}{2W}\left[F_1 + F_2 + (W+M)F_3 + (W-M)F_4 \right. \\
&\qquad \left. - \frac{1}{2}(\mu^2-t)\left(\frac{F_3}{W-M} + \frac{F_4}{W+M}\right)\right] \\
A_4 &= \frac{1}{2W}\left[F_1 + F_2 - \frac{1}{2}(\mu^2-t)\left(\frac{F_3}{W-M} + \frac{F_4}{W+M}\right)\right],
\end{aligned}\right\} \tag{4-7}$$

where W, E_1 and E_2 are the total energies of the pion nucleon system, the target nucleon and the final nucleon in the CM system, respectively. M and μ are masses of nucleon and pion, respectively. The real parts of the invariant amplitudes are obtained using the fixed-t dispersion relation as follows,

$$\begin{aligned}
\mathrm{Re}\, A_i^{(\pm,0)}(s,t) = B_i^{(\pm,0)}(s,t) + \frac{P}{\pi}\int_{(M+u)^2}^{\infty}\left(\frac{\mathrm{Im}\, A_i^{(\pm,0)}(s',t)}{s'-s}\right. \\
\left. + \xi_i \cdot \frac{\mathrm{Im}\, A_i^{(\mp,0)}(s',t)}{s'-u}\right)ds',
\end{aligned} \tag{4-8}$$

where $B_i^{(\pm,0)}(s,t)$ represents the Born term. Symbols s, t and u are usual Mandelstam variables. ξ_i is 1 for $i=1$, 2 and 4 and $\xi_i=-1$ for $i=3$. The superfix $+$, $-$ and 0 represents the processes $\gamma+\mathrm{p}\to\pi^+ + \mathrm{n}$, $\gamma+\mathrm{n}\to\pi^- + \mathrm{p}$ and $\gamma+\mathrm{p}\to\pi^\circ + \mathrm{p}$, respectively. In the calculation, the imaginary parts of the invariant amplitudes in the un-

physical region were obtained by the analytical continuation. After obtaining real parts, the invariant amplitudes are transformed to the helicity amplitudes by the relations;

$$\left.\begin{aligned} F_1 &= A_1 + (W-M)A_4 + \frac{(\mu^2-t)}{2(W-M)}(A_3-A_4) \\ F_2 &= -A_1 + (W+M)A_4 + \frac{(\mu^2-t)}{2(W+M)}(A_3-A_4) \\ F_3 &= (W-M)A_2 + A_3 - A_4 \\ F_4 &= -(W+M)A_2 + A_3 - A_4 . \end{aligned}\right\} \tag{4-9}$$

Finally, the helicity amplitudes are obtained with the following relations;

$$\mathfrak{F}_i = F_i \cdot \chi_i \quad (i=1, \ldots, 4), \tag{4-10}$$

$$\left.\begin{aligned} H_1 &= -\sqrt{2}\sin\frac{\theta}{2}\cdot\cos^2\frac{\theta}{2}(\mathfrak{F}_3+\mathfrak{F}_4) \\ H_2 &= \sqrt{2}\cos\frac{\theta}{2}\{(\mathfrak{F}_2-\mathfrak{F}_1)+\sin^2\frac{\theta}{2}(\mathfrak{F}_3-\mathfrak{F}_4)\} \\ H_3 &= \sqrt{2}\sin^2\frac{\theta}{2}\cdot\cos\frac{\theta}{2}(\mathfrak{F}_3-\mathfrak{F}_4) \\ H_4 &= \sqrt{2}\sin\frac{\theta}{2}\{(\mathfrak{F}_2+\mathfrak{F}_1)+\cos^2\frac{\theta}{2}(\mathfrak{F}_3+\mathfrak{F}_4)\}. \end{aligned}\right\} \tag{4-11}$$

The observables are calculated from these amplitudes as follows;

$$\frac{d\sigma}{d\Omega^*} = \frac{1}{2}\cdot\frac{q}{k}\sum_{i=1}^{4}|H_i|^2 \tag{4-12}$$

$$\Sigma = \frac{q}{k}\cdot\frac{1}{\frac{d\sigma}{d\Omega^*}}\cdot \mathrm{Re}\,(H_1\cdot H_4^* - H_2\cdot H_3^*) \tag{4-13}$$

$$T = \frac{q}{k}\cdot\frac{1}{\frac{d\sigma}{d\Omega^*}}\cdot \mathrm{Im}\,(H_1\cdot H_2^* + H_3\cdot H_4^*) \tag{4-14}$$

$$P = -\frac{q}{k}\cdot\frac{1}{\frac{d\sigma}{d\Omega^*}}\cdot \mathrm{Im}(H_1\cdot H_3^* + H_2\cdot H_4^*). \tag{4-15}$$

In the calculation of integrals of the equation (4–8), the region of the integration was cut at $s_{max}=5.5$ (GeV)^2. The effect of this cut was tested by changing s_{max} from 3.5 to 5.5 (GeV)^2. The cut energy of $s_{max}=5.5$ (GeV)^2 is considered to be good as shown in Fig. 18. Similar result was also obtained by Barbour, Malone and Moorhouse in the case of charged pion photoproduction.[18]

The values of the photon coupling of resonances obtained by MW listed in Table 7 were used and the observables were calculated. The results are shown in Fig. 19 and give the smaller cross sections than the present experiment at forward angles below 600 MeV as same as the analyses by MW and MOR. In order to improve the situation, the photon couplings of the resonances except the $P_{33}(1232)$ resonance were modified. This modification did not thoroughly improve the fitting to the present data. Then the resonance saturation of imaginary parts was practically

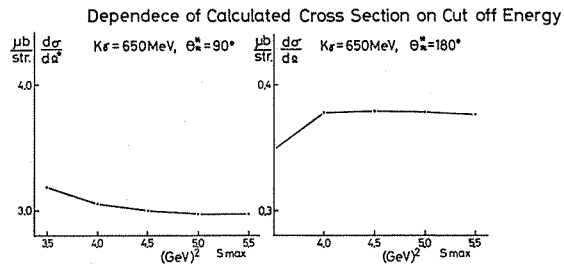

Fig. 18. Effect of the cut energy s_{max} to the dispersion integral.

Table 7. Resonance Parameters by Metcalf and Walker used in the present calculation.

Resonance $L_{2I,2J}$	Energy W_0 (MeV)	Width Γ_0 (MeV)	l	j_r	X (MeV)	Helicity Element	Photon Coupling $(\mu b)^{1/2}$ $A^{(+)}(s_0)$	$A^{(-)}(s_0)$
S_{11}	1530	100	0	1	350	A_{0+}	0.600	−0.480
S_{31}	1660	150	0	1	350	A_{0+}	0.500	−0.500
S_{11}	1700	150	0	1	350	A_{0+}	0.110	−0.170
P_{11}	1430	230	1	1	350	A_{1-}	0.600	−0.370
P_{11}	1650	160	1	1	350	A_{1-}	0.370	−0.260
P_{31}	1850	230	1	1	350	A_{1-}	0.100	−0.100
P_{33}	1233	120	1	1	185	A_{1+}	−1.200	1.200
						B_{1+}	2.250	−2.520
P_{33}	1670	120	1	1	350	A_{1+}	0.000	0.000
						B_{1+}	0.000	0.000
D_{13}	1510	120	2	1	350	A_{2-}	0.050	0.525
						B_{2-}	1.510	−1.080
D_{13}	1730	130	2	1	350	A_{2-}	0.000	0.000
						B_{2-}	0.000	0.000
D_{15}	1650	140	2	2	350	A_{2+}	0.050	0.020
						B_{2+}	−0.141	0.030
F_{15}	1690	135	3	2	350	A_{3-}	0.050	−0.050
						B_{3-}	0.560	0.000
F_{35}	1880	250	3	2	350	A_{3-}	−0.071	0.071
						B_{3-}	−0.030	0.030
F_{37}	1925	200	3	3	350	A_{3+}	−0.141	0.141
						B_{3+}	0.115	−0.115

In the notation of this paper, the sign of the amplitudes of the process $\gamma+p\rightarrow\pi^++n$ have opposite sign to those of MW's analysis.

modified. However, it should be noted that the results of the present calculation with resonance saturation of imaginary parts for the process $\gamma+p\rightarrow\pi^++n$ reproduced well the experimental results on the cross section, target asymmetry and polarized beam asymmetry. The analysis by MW contains a large background amplitude in the imaginary part of the S wave (Im A_{0+}) as shown in Fig. 20. The analysis by Devenish, Lyth and Rankin (DLR)[19] based on the dispersion relation also included an additional amplitude to the imaginary part of the S wave by the requirement of unitarity imposed by the Watson theorem.[20] The recent analysis by Noelle[21] also includes background in the S and P waves multiplying S-matrix by a phase factor for elastic initial and final state interaction. Therefore, the additional amplitude was introduced in Im A_{0+} for the process $\gamma+p\rightarrow\pi^\circ+p$. The shape with a Breit-Wigner type was adopted to this background amplitude for the simplicity. The parameters of the

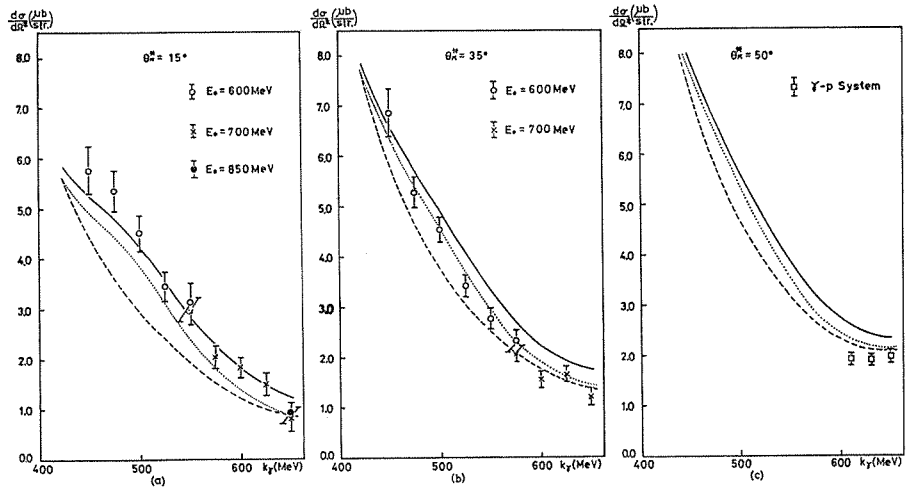

Fig. 19. The energy dependence of the cross sections between 450 MeV and 650 MeV at the CM angle of (a) 15°, (b) 35° and (c) 50°. Soild and dashed curves represent the results of the present analysis using the photon couplings given by MW with and without the additional imaginary S wave background amplitude, respectively. The parameters of this background amplitude are W=1330 MeV, Γ_0=100 MeV and peak height is 0.58 $(\mu b)^{1/2}$. As an example of modification of the photon coupling, the dotted curve represents the result of the present calculation when the photon coupling of the $S_{31}(1660)$ resonance is set to be zero after adding the background amplitude.

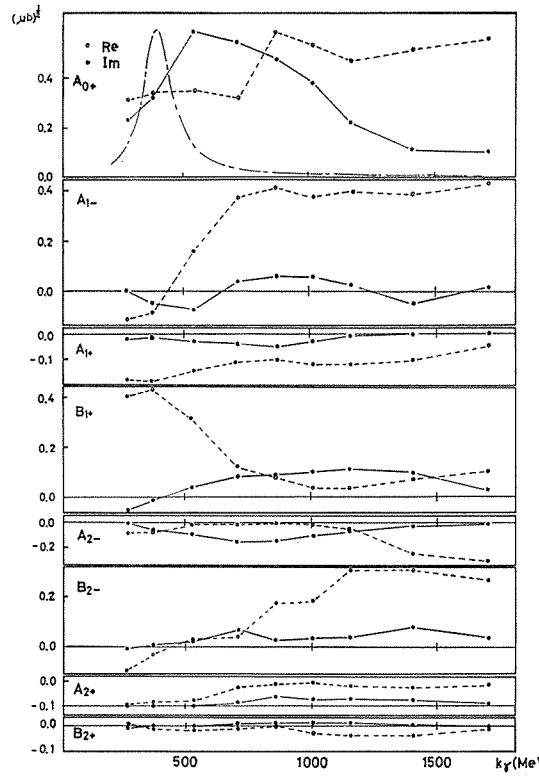

Fig. 20. Background amplitudes for the process $\gamma+p\rightarrow\pi^0+p$ given by MW. The background amplitude in ImA_{0+} in the present calculation is also shown by dash-dotted curve.

shape were the peak height, the peak position and the width and they used values of 0.58 $(\mu b)^{1/2}$, 1330 MeV (corresponded to $k_\gamma = 475$ MeV) and 100 MeV, respectively. These parameters were not obtained by the χ^2-search procedure, but the small changes of these values by hand were executed. The result seems to give a fairly good agreement with the present data as is shown in Fig. 19 by the solid curves. It was also found that the modification of the photon couplings of the $S_{11}(1530)$ and $S_{31}(1660)$ resonances after adding the above background amplitude improved the fitting to the present data of forward cross sections above 550 MeV as shown in Fig. 19 by dotted curves. However, modification of these couplings will give rather large effects on the observables at higher energies and are outside the present scope. The effect of the present additional background amplitude to the other observables was also calculated and the polarized target asymmetry T at $\theta_\pi^* = 30°$ and 80° is shown in Fig. 21. This background amplitude shifted down the calculated values of T around 450 MeV toward the experimental data.[22] Therefore this additional background amplitude is expected to shift down the predicted values of T by MOR toward the experimental values when included to that analysis, because the prediction by MOR lies above the experimental values.

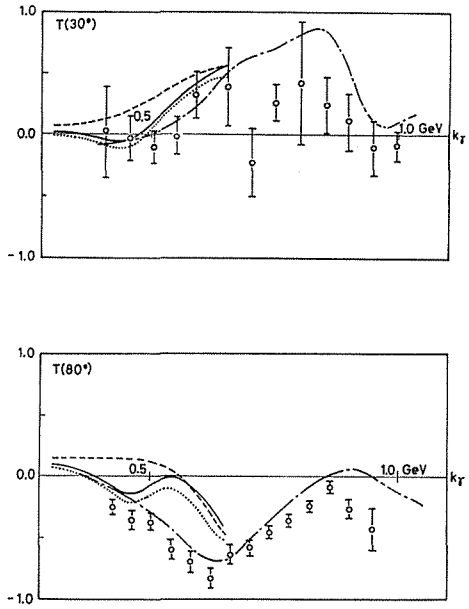

Fig. 21. Comparison of the present calculation with the experimental data of polarized target asymmetry. Data are taken from M. Fukushima et al.[22] and the solid, dashed and dotted curves are as same as Fig. 19. The dash-dotted curve represents the prediction by MOR.

About the problem of a convergence of the partial wave expansion, it is known that the cut off of the partial wave expansion at some angular momentum gives a good approximation in a region of $|t| < 1.5$ (GeV/c)^2 for π° photoproduction.[19] Therefore in this low energy and forward anglar region, the convergence seems to be assured.

Finally the following conclusions can be drawn. The present results on the cross sections of the process $\gamma + p \to \pi^\circ + p$ between 450 MeV and 975 MeV and in the

angular region from 15° to 50° measured with the "π^0-system" are consistent with the measurement with the "γ–p system" at the overlap region. The results are also consistent with the previous measurement by Y. Hemmi et al., P. Dougan et al. and H. De Staebler et al. at the overlap regions. The recent partial wave analyses by MW and MOR reproduced well the present results except the data in the energy region below 600 MeV and at forward angles of 15° and 35°. A simple analysis based on the fixed-t dispersion relation with resonance saturation of imaginary parts indicates that this discrepancy cannot be explained by adjusting the photon couplings of the resonances. It requires the additional background amplitude for the imaginary part of the S wave for the process $\gamma+\mathrm{p}\rightarrow\pi^0+\mathrm{p}$ around 500 MeV.

ACKNOWLEDGEMENT

The author would like to express his sincere thanks to Professors K. Miyake, T. Nakamura and S. Kato for their continuous encouragements and guidances throughout this work.

He is deeply grateful to Dr. K. Ukai for his continuous encouragement and fruitful discussion. He is also grateful to Dr. M. Yoshioka who is a good partner throughout the experiment and his work at every stage of the experiment is greatly appreciated.

The experiment was executed by Professors K. Miyake, T. Nakamura, S. Kato, Drs. R. Kikuchi, Y. Hemmi, K. Ukai, M. Yoshioka, K. Toshioka and M. Daigo, Messrs. M. Ono, K. Sugano, M. Chiba, M. Minowa, Y. Suzuki, T. Shimomura, Y. Hoshi, T. Shinohara and the author. The author would like to express his gratitude to all of the collaborators.

He is also indebted to Dr. Y. Inagaki and late Dr. N. Yamashita for their support and suggestions at the preparing stage of the experiment.

He wishes to express his thanks to Messrs. A. Imanishi, T. Kitami, K. Shiino, K. Watanabe and the members of machine shop at INS for their preparation of equipments.

Thanks are also due to the synchrotron crew at INS under the leadership of Professors S. Yamaguchi, K. Huke and K. Yoshida for their nice operation.

Finally the author would like to express his gratitude to Mrs. H. Katayama for nice typing of the manuscript and Miss A. Sato and Messr. M. Yoshizawa for a neat preparation of figures.

The data reduction and numerical calculation was performed with TOSBAC–3400 at INS nd HITAC–8700 at KEK.

REFERENCES

1) F. A. Berends and A. Donnachie, Nucl. Phys. **B136** (1978) 317.
2) W. J. Metcalf and R. L. Walker, Nucl. Phys. **B76** (1974) 253.
3) R. G. Moorhouse, H. Oberlack and A. Rosenfeld, Phys. Rev. **D9** (1974) 1.
4) P. Feller, M. Fukushima, N. Horikawa, R. Kajikawa, K. Mori, T. Nakanishi, T. Oshima, C. O. Pak, M. Saito, S. Suzuki, Y. Tarui, T. Matsuda, K. Mizushima and N. Tokuda, Nucl. Phys. **B104** (1976) 219.
5) R. C. E. Devenish, D. H. Lyth and W. A. Rankin, Phys. Letters **52B** (1974) 227.
6) R. L. Crawford, Nucl. Phys. **B97** (1975) 125.
7) I. M. Barbour and R. L. Crawford, Nucl. Phys. **B111** (1976) 358.

8) I. M. Barbour, R. L. Crawford and N. H. Parsons, Nucl. Phys. **B141** (1978) 253.
9) M. Yoshioka, Memoirs of the Faculty of Science, Kyoto University, Series A of Physics, Astrophysics, Geophysics and Chemistry **35** (1980) 297.
10) L. Tau, Nucl. Insr. Methods **34** (1965) 352.
11) N. Yamashita, Memoirs of the Faculty of Science, Kyoto University, Series A of Physics, Astrophysics, Geophysics and Chemis try **35** (1977) 35.
12) T. Miyachi, Y. Akino, K. Gomi, A. Kusumegi, M. Mishina, H. Okuno, I. Sato, M. Takeda and M. Yoshioka, J. Phys. Soc. Japan **33** (1972) 577.
13) L. I. Shiff, Phys. Rev. **83** (1951) 252.
14) Y. Hemmi, T. Inagaki, Y. Inagaki, A. Maki, K. Miyaki, T. Nakamura, N. Tamura, J. Tsukamoto, N. Yamashita, H. Itoh, S. Kobayashi, S. Yasumi and H. Yoshida, Phys. Letters **B43** (1973) 79.
15) P. Dougan, V. Ramsay and W. Stiefler, Z. Phys. **A276** (1976) 155.
16) H. De Staebler, Jr., E. F. Ericson, A. C. Hearn and C. Schaerf, Phys. Rev. **140** (1965) B336.
17) R. L. Walker, Phys. Rev. **182** (1969) 1729.
18) I. Barbour, W. Malone and R. G. Moorhouse, Phys. Rev. **D4** (1971) 1521.
19) R. L. E. Devenish, D. H. Lyth and W. A. Rankin, Daresbury Report DNPL/P109 (1972).
20) K. M. Watson, Phys. Rev. **95** (1954) 228.
21) P. Noelle, Nagoya University Preprint DPNU–15–77 (1977).
22) M. Fukushima, N. Horikawa, R. Kajikawa, H. Kobayakawa, K. Mori, T. Nakanishi, C. O. Pak, S. Suzuki, T. Matsuda, N. Tokuda, M. Daigo and T. Oshima, Nucl. Phys. **B136** (1978) 189.